Journal of Non-Newtonian Fluid Mechanics 214 (2014) 57–68

Contents lists available at ScienceDirect

Journal of Non-Newtonian Fluid Mechanics

journal homepage: http://www.elsevier.com/locate/jnnfm

A new viscoelastic benchmark flow: Stationary bifurcation in a cross-slot

F.A. Cruz [a], R.J. Poole [b], A.M. Afonso [a], F.T. Pinho [c], P.J. Oliveira [d], M.A. Alves [a,*]

[a] Departamento de Engenharia Química, CEFT, Faculdade de Engenharia da Universidade do Porto, Rua Dr. Roberto Frias, 4200-465 Porto, Portugal
[b] School of Engineering, University of Liverpool, Brownlow Street, Liverpool L69 3GH, United Kingdom
[c] CEFT, Departamento de Engenharia Mecânica, Faculdade de Engenharia, Universidade do Porto, Rua Dr. Roberto Frias, 4200-465 Porto, Portugal
[d] Departamento de Engenharia Electromecânica, C-MAST, Universidade da Beira Interior, 6201-001 Covilhã, Portugal

ARTICLE INFO

Article history:
Received 10 October 2013
Received in revised form 26 September 2014
Accepted 29 September 2014
Available online 6 October 2014

Keywords:
Finite-volume method
Cross-slot flow
Elastic instabilities
Benchmark flow
Flow transitions

ABSTRACT

In this work we propose the cross-slot geometry as a candidate for a numerical benchmark flow problem for viscoelastic fluids. Extensive data of quantified accuracy is provided, obtained via Richardson extrapolation to the limit of infinite refinement using results for three different mesh resolutions, for the upper-convected Maxwell, Oldroyd-B and the linear form of the simplified Phan-Thien–Tanner constitutive models. Furthermore, we consider two types of flow geometry having either sharp or rounded corners, the latter with a radius of curvature equal to 5% of the channel's width. We show that for all models the inertialess steady symmetric flow may undergo a bifurcation to a steady asymmetric configuration, followed by a second transition to time-dependent flow, which is in qualitative agreement with previous experimental observations for low Reynolds number flows. The critical Deborah number for both transitions is quantified and a set of standard parameters is proposed for benchmarking purposes.

1. Introduction

Arratia et al. [1] demonstrated experimentally that the low-Reynolds number (Re) flow of a flexible polymer solution (a polyacrylamide aqueous solution) through a microfluidic cross-slot geometry can give rise to two different instabilities: a first instability, in which the flow remains steady but becomes spatially asymmetric; and a second instability, in which the flow becomes unsteady and fluctuates with time. In fact, such asymmetries, which are purely-elastic in nature, are not new and were also present in the early experimental work of Gardner et al. [2]. Although the photon-correlation velocimetry technique used by Gardner and co-workers was rather noisy, their velocity profiles are clearly asymmetric downstream of the cross-slot. Gardner et al. [2] thought that the asymmetry was a consequence of either imperfections in the geometry or a "fluidic-type" instability. These experimental results were the stimuli for our own numerical investigations. In Poole et al. [3], a finite-volume numerical technique was used to show that such asymmetries could be predicted even for the upper-convected Maxwell (UCM) model in a truly-inertialess flow ($Re \to 0$), and that they were probably a consequence of the high compressive normal stresses developed by the viscoelastic fluid when the two incoming streams join. These normal stresses lead to a concave velocity profile, together with an inflection point, as illustrated in [3] along the diagonal lines $y = \pm x$. It is well known that inflection points in velocity profiles are a necessary condition for inviscid instabilities, but even with viscous fluids inflection points are often associated with flow instabilities, at least in flows with non-negligible inertia (a famous example are the experiments and theoretical predictions of G.I. Taylor in rotating Couette flows [4] – now known as Taylor–Couette flows). However, this association is empirical at best, lacking the mathematical/physical insight quality of the Rayleigh criterion for inviscid instabilities, and should thus be regarded with caution.

In this work, we propose the two-dimensional (2D) cross-slot geometry, illustrated schematically in Fig. 1, as an interesting and useful candidate for a numerical benchmark case for viscoelastic fluid flows. For a wide range of differential viscoelastic models, namely the UCM and Oldroyd-B models [5] and the Phan-Thien and Tanner (PTT) model [6], we show that, in the limit of negligible inertia, *i.e.* when Re approaches zero, the flow exhibits two different types of purely-elastic instabilities. Above a first critical value of the Deborah number, $De = \lambda U/D = \lambda Q/D^2$, where λ is the fluid relaxation time, U the bulk velocity in each arm, Q the flow rate per unit depth in each arm and D the channel width, the steady flow becomes spatially asymmetric, even though the geometry is perfectly symmetric; at higher De the flow then becomes time-dependent. The geometry is simple and the steady asymmetric flow is well defined. The local evolution of the bifurcation parameter DQ [3] is well described by a square-root fit which is typical of supercritical pitchfork bifurcations, $DQ = A\sqrt{De - De_{CR}}$, and the

* Corresponding author. Fax: +351 22 5081449.
E-mail address: mmalves@fe.up.pt (M.A. Alves).

http://dx.doi.org/10.1016/j.jnnfm.2014.09.015
0377-0257/

critical Deborah number, De_{CR}, can be predicted with high accuracy, based on the Richardson extrapolation of results for systematically-refined meshes. In addition the flow contains an internal stagnation point where a fluid element is subjected to large extensional stresses. Such behaviour allows the accuracy of numerical methods to be tested away from any influence of boundary conditions, namely by analysis of the mesh-wise convergence of the local Weissenberg number, $Wi_o = \lambda\dot{\varepsilon}_o$, calculated at the stagnation point. Indeed, rounding the corners of the cross-slot with a small radius of curvature seems to have little to no influence on the pitchfork bifurcation, as will be shown in the results section.

Up until the work by Arratia et al. [1], although a great deal of research had been conducted using stagnation point geometries similar to the cross-slot device, such as the four roll mill and opposed-jet devices, such steady asymmetries have largely gone unreported. Therefore, we do not present a detailed review of the early literature here. The interested reader is referred to Schoonen et al. [7] and Remmelgas et al. [8]. For in-depth reviews of the early literature on elastic instabilities see [9,10]. In numerical studies the inability to predict steady asymmetric flow is easily explained, since most studies imposed symmetry boundary conditions to reduce the computational burden (*e.g.* [7,8]). Experimentally it is likely that the main reason why such instabilities have not been observed is the relative unimportance of elastic effects in macro-sized devices, when compared to their micro-sized counterparts (*cf.* definition of *De*). The microfluidic nature of the experiments of both Arratia et al. [1] and Gardner et al. [2], in which effects due to elasticity are inherently enhanced given the small length scales of the flow, is the main reason why such instabilities became observable. Of course the paper by Gardner and co-workers predates the term "microfluidics" by some decades, but their channel width, $D = 250\ \mu m$, is actually *smaller* than in the work of Arratia et al., at $D = 650\ \mu m$. This argument is further supported by experimental results for surfactant flows, published by Pathak and Hudson [11] in the same year as Arratia et al. [1], again in a microfluidic geometry, in which the steady asymmetry and subsequent transition to time-dependent flow were also observed. Since 2006, other publications have reported steady-state asymmetries in cross-slot flows of wormlike micellar solutions, including fully asymmetric flow [11,12], *Wi-Re* stability diagrams delimiting different flow behaviours [12,13] and also the formation of lip vortices in the inlet channels for strongly viscoelastic fluids [12,14].

With the increasing prevalence of microfluidic devices in viscoelastic fluid flow research and engineering, in recent years a number of publications have addressed the issue of steady asymmetries in various cross-slot flows of polymeric solutions. Rocha et al. [15] simulated FENE-CR and FENE-P fluid flows and predicted a transition to steady asymmetry at progressively lower *De* with increasing values of the extensibility parameter and polymer concentration. The effect of corner sharpness was not significant up to a radius of curvature of 50% of the channel width. According to Larson et al. [16] and later McKinley et al. [17], streamline curvature is required for the onset of elastic instabilities. This curvature may either be intrinsic to the geometric confinement

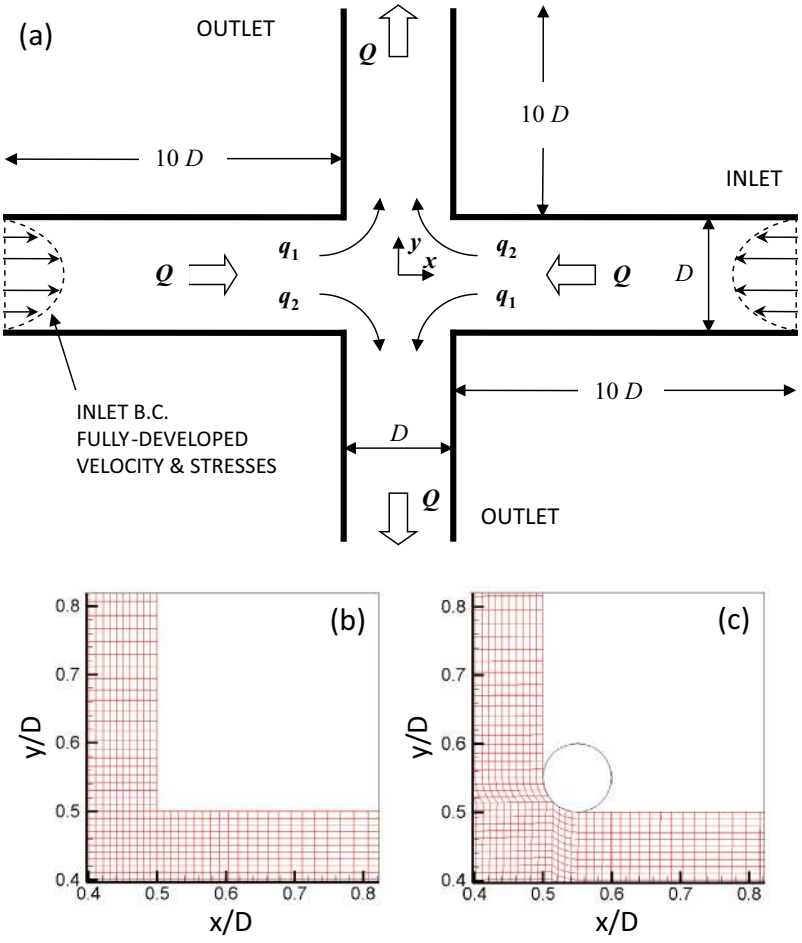

Fig. 1. (a) Schematics of the cross-slot geometry. Zoomed view of the meshes near the corners of the (b) sharp and (c) rounded geometries, for meshes M2-R0 and M2-R5, respectively (see Table 1 for details). The rounded corner has a radius of curvature of 5% of the channel width, as illustrated by the superimposed circle in (c).

of the fluid, as in Taylor–Couette flows, or be a by-product of the flow itself, as in the cross-slot geometry, such that rounding the cross-slot corners has a negligible effect on the radius of curvature of streamlines near the centre of the device [15].

Oliveira et al. [18] simulated the flow of UCM and PTT fluids in a flow-focusing device based on the cross-slot geometry. By manipulation of velocity and width ratios of the three inlet channels, they showed flow transitions directly from a steady symmetric to an unsteady state if the normal stresses near the stagnation point are not sufficiently high, suggesting the transition to steady asymmetric flow is a stress relief mechanism. Interestingly, in their simulation of cross-slot flows undertaken using the FENE-P model, Xi and Graham [19] did not report steady asymmetries, but instead a direct transition to unsteady flow at high *De*. The viscosity ratio used in their study, $\beta = \eta_s/(\eta_s + \eta_p) = 0.95$, corresponds to a dilute polymer solution. Therefore, it is possible this particular flow simulation does not generate sufficiently-high normal stresses and foregoes the steady asymmetric configuration, even though the extensibility parameter $b = 1000$ is typical of a high molecular weight polymer. Interestingly, Rocha et al. [15] quantified the dependence of De_{CR} on both viscosity ratio β and extensibility parameter $L^2 = b + 5$ simultaneously, and found that this critical value decreases exponentially with $L^2(1-\beta)/\beta$, which demonstrates how polymer molecules must be both sufficiently abundant and sufficiently long if steady asymmetric flow patterns are to be observed. Additionally, Afonso et al. [20] simulated three-dimensional (3D) cross-slot flows with the UCM model. Steady asymmetries were observed for uniaxial extension, but not for biaxial extension. Noticeably, the normal-stress values for components aligned with the outlet channels – *e.g.* in uniaxial extension, if the inlet channels are along *y*- and *x*-directions, the normal stress component aligned with the outlet channel is τ_{zz} – near the stagnation point are up to two orders of magnitude higher in the uniaxial case.

Besides curvature and sufficiently high polymer concentration and molecular weight, a further requirement for symmetry breaking in stagnation point flows seems to be the occurrence of a free stagnation point, as reported by Soulages et al. [21]. Using experimental measurements and simulations of Oldroyd-B and simplified linear PTT fluids, in T-shaped microchannels with two opposing inlets, and an orthogonal outlet arm, the authors tested the influence of an added cavity, located opposite to the direction of the outlet. In the absence of this cavity, the stagnation point is pinned to the microchannel wall, and even though normal stresses at the observed birefringence strand are 3-fold higher without the cavity, symmetry breakage is only seen in the channel with the recirculation cavity, in which the stagnation point is detached from the wall. Furthermore, without the cavity, the transition to time-dependent flow happens at lower *Wi*, in agreement with the previous discussion on the stress relief provided by a transition to steady asymmetric flow. As pointed out by Soulages et al. [21], the need for a free stagnation point seems to be related to streamline distortion near that point, and the non-zero strain rate at the stagnation point in the microchannel with cavity, contrasting with zero strain rates at wall stagnation points.

Table 1
Characteristics of the computational meshes. NC – number of cells; DOF – degrees of freedom; RCC – radius of curvature of corners; *D* – channel width.

Mesh	NC	DOF	RCC	$\frac{\Delta x_{min}}{D} = \frac{\Delta y_{min}}{D}$
M1-R0	12,801	76,806	0	0.02
M2-R0	50,601	303,606	0	0.01
M3-R0	201,201	1,207,206	0	0.005
M1-R5	12,801	76,806	0.05 *D*	0.02
M2-R5	50,601	303,606	0.05 *D*	0.01
M3-R5	201,201	1,207,206	0.05 *D*	0.005

It is clear from the previous description that the cross-slot flow has unique features absent in other benchmark flows, namely in the 4:1 sudden contraction [22] or the flow around a confined cylinder [23]. The latter is essentially dominated by shear, except in the vicinity of the upstream and downstream stagnation points, and although extensional flow plays an important role in the 4:1 contraction, this flow also contains an important shear contribution and a strong dependence on the boundary conditions, namely on the effect of the re-entrant corner. In contrast, the main feature of the cross-slot flow is its strong extensional nature in a region far away from walls, even if there are shear effects elsewhere. The possible occurrence of steady flow asymmetries, which are very sensitive to fluid rheology, flow conditions and numerical accuracy, is also a unique characteristic of cross-slot flows. Indeed, we are not alone in considering the cross-slot bifurcation as an important unsolved problem [24]. Interestingly, upon flow bifurcation, the stagnation point becomes the centre of a small shear dominated area surrounded by the larger extensional field. To the best of our knowledge, the only attempt at addressing a related problem through linear stability analysis [25] was able to predict instability in the idealized centreline for Oldroyd-B type fluids, but only for short waves out of the plane of flow. In contrast, the perturbations seen in our study all lie within the plane of flow. Considering the date of the aforementioned paper, this problem has stood unsolved for circa 30 years, and particularly in the past 8 years, despite renewed efforts since Arratia et al. [1] rediscovered experimentally the phenomenon. Furthermore, the classical benchmark problems lack a well-defined point beyond which they become unstable, whereas for the cross-slot this transition is very well defined and leads to a new type of instability corresponding to a supercritical bifurcation from steady symmetric to steady asymmetric flow. All factors considered, we regard the cross-slot flow as a unique and challenging problem, worthy of benchmark status.

2. Governing equations, numerical method and meshes

To model the cross-slot flow we assume that the flow is inertialess ($Re \to 0$), two-dimensional, isothermal and incompressible. Under these conditions, the equations that need to be solved are those of conservation of mass,

$$\nabla \cdot \mathbf{u} = 0, \tag{1}$$

and the momentum equation,

$$-\nabla p + \nabla \cdot \boldsymbol{\tau} + \eta_s \nabla^2 \mathbf{u} = \mathbf{0}, \tag{2}$$

together with a suitable equation for the viscoelastic extra-stress tensor $\boldsymbol{\tau}$. We choose here to use the well-known model due to Phan-Thien and Tanner [6,26] – in its simplified, linearized form often denoted sPTT – of which the UCM and Oldroyd-B models are limiting cases

$$\left(1 + \frac{\lambda\varepsilon}{\eta_p}\mathrm{Tr}(\boldsymbol{\tau})\right)\boldsymbol{\tau} + \lambda\left[\frac{\partial \boldsymbol{\tau}}{\partial t} + \nabla \cdot \mathbf{u}\boldsymbol{\tau}\right] = \eta_p(\nabla \mathbf{u} + \nabla \mathbf{u}^T) + \lambda(\boldsymbol{\tau} \cdot \nabla \mathbf{u} + \nabla \mathbf{u}^T \cdot \boldsymbol{\tau}). \tag{3}$$

In these equations the constant model parameters are the relaxation time of the polymer λ, the zero-shear-rate polymer viscosity η_p, the solvent viscosity η_s, and the extensibility parameter ε. For both the Oldroyd-B and sPTT models, the viscosity ratio β, defined as the ratio of solvent viscosity to total zero-shear-rate viscosity ($\eta_0 = \eta_s + \eta_p$), was kept constant at $\beta = \eta_s/\eta_0 = 1/9$. Two typical values of extensibility parameter ε are used to assess its effect, $\varepsilon = 0.02$ and $\varepsilon = 0.25$ (note that extensibility is larger for lower values of ε). Although a number of shortcomings exist with both the UCM and Oldroyd-B models, most notably the unbounded nature of the

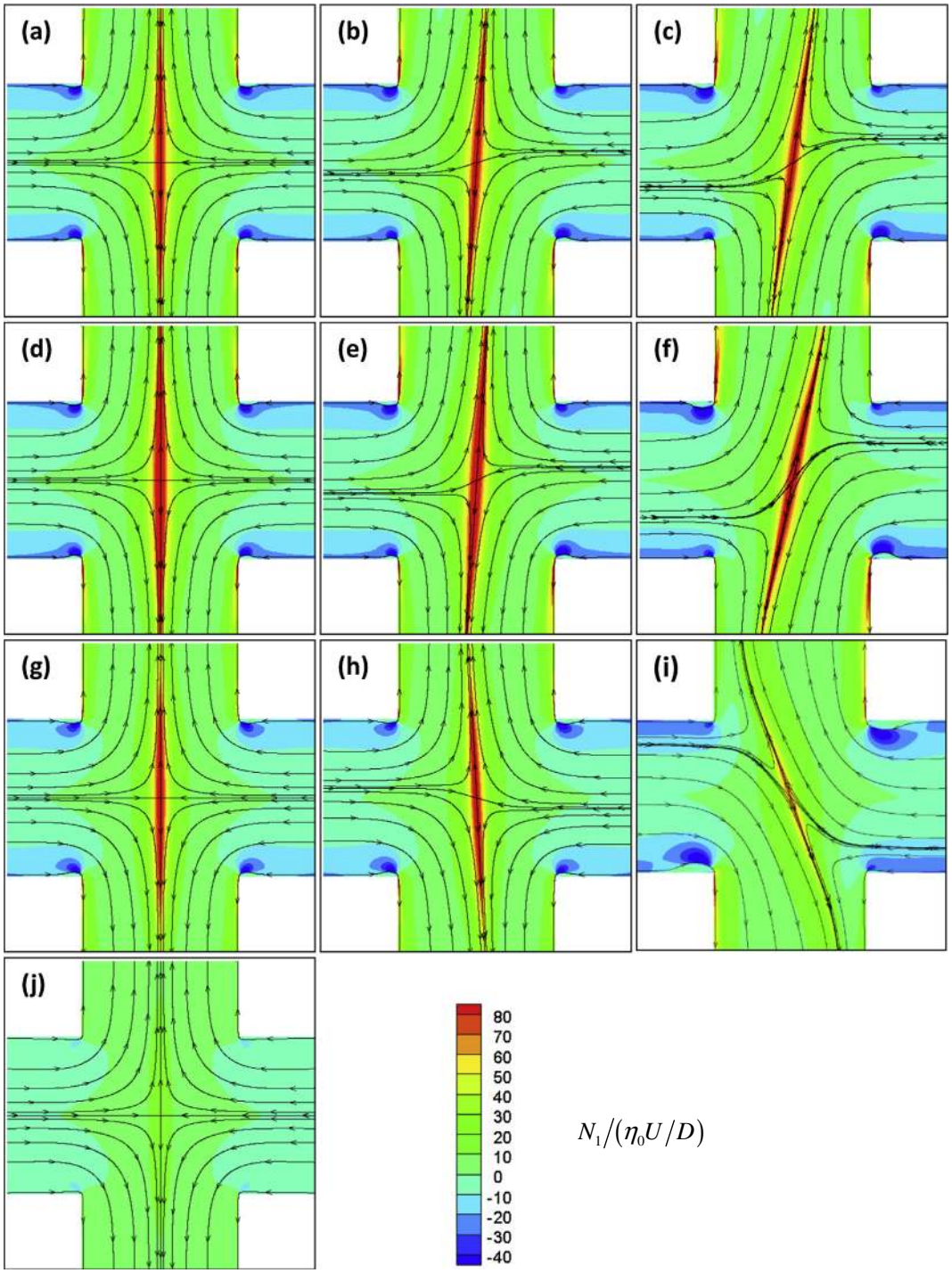

Fig. 2. Streamline patterns superimposed onto contour plots of the normalized polymeric first normal stress difference $(\tau_{yy} - \tau_{xx})/(\eta_o U/D)$. Represented are the highest *De* steady-state symmetric cases (left column), the lowest *De* steady-state asymmetric cases (middle column) and the highest *De* steady-state asymmetric cases prior to transition to time-dependent flow (right column): UCM model at (a) *De* = 0.31, (b) *De* = 0.315 and (c) *De* = 0.33; Oldroyd-B model with $\beta = 1/9$ at (d) *De* = 0.36, (e) *De* = 0.37 and (f) *De* = 0.42; sPTT model with $\beta = 1/9$ and $\varepsilon = 0.02$ at (g) *De* = 0.50, (h) *De* = 0.51 and (i) *De* = 0.92. Noteworthy, the first normal stress difference reaches its maximum value at the highest *De* prior to the onset of steady asymmetric flow, with subsequent post-transition stress relief. Results for the (j) sPTT model with $\beta = 1/9$ and $\varepsilon = 0.25$ at *De* = 1.20, the highest simulated *De*, are also provided. Illustrations are provided for calculations on mesh M3-R0 (see Table 1 for details).

steady-state extensional stresses above a critical strain rate $\dot{\varepsilon} = 1/(2\lambda)$ and their inability to predict shear-thinning behaviour, they are probably the simplest differential models of an elastic fluid which can capture qualitatively many features of highly-elastic flows (*e.g.* [27,28]). These particular deficiencies are absent in the sPTT model.

A fully implicit, second-order, finite-volume numerical method is applied to solve the governing equations. The log-conformation technique, introduced by Fattal and Kupferman [29], is used to solve Eq. (3), after it is converted to the log-conformation tensor as detailed in [30]. The original numerical method and subsequent developments have been described in great detail elsewhere [30–32], and so are not unnecessarily repeated here. Boundary conditions for the traction vector components at the walls, which are needed to evaluate the stress divergence term in the momentum equation, are based on local analytical solutions. With

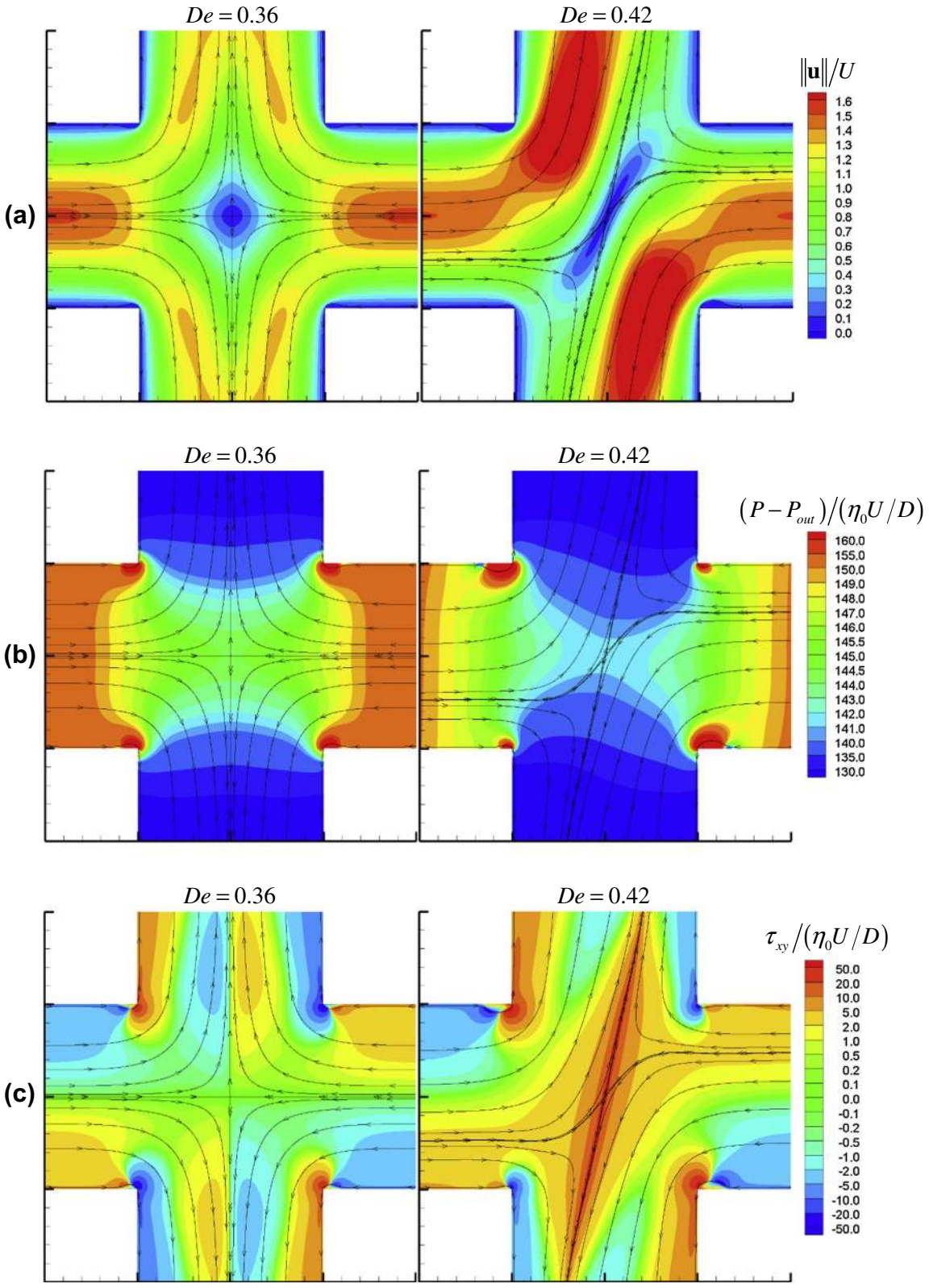

Fig. 3. Contour plots, with superimposed streamlines, of normalized: (a) velocity magnitude $||\mathbf{u}||$; (b) relative pressure $P - P_{out}$; (c) extra-stress component τ_{xy}. Data is provided for the Oldroyd-B model with $\beta = 1/9$ at $De = 0.36$, the highest steady symmetric case, and $De = 0.42$, the highest steady asymmetric case. Illustrations are provided for calculations on mesh M3-R0 (see Table 1 for details).

the present constitutive models, these are equivalent to assuming a viscometric flow along the wall planes. No finite disturbances are introduced in the numerical simulations to induce the onset of flow asymmetries. Instead, asymmetric solutions were found to develop naturally in the simulations, most likely from accumulation of round-off error at machine level precision – we use double precision in Fortran for all calculations.

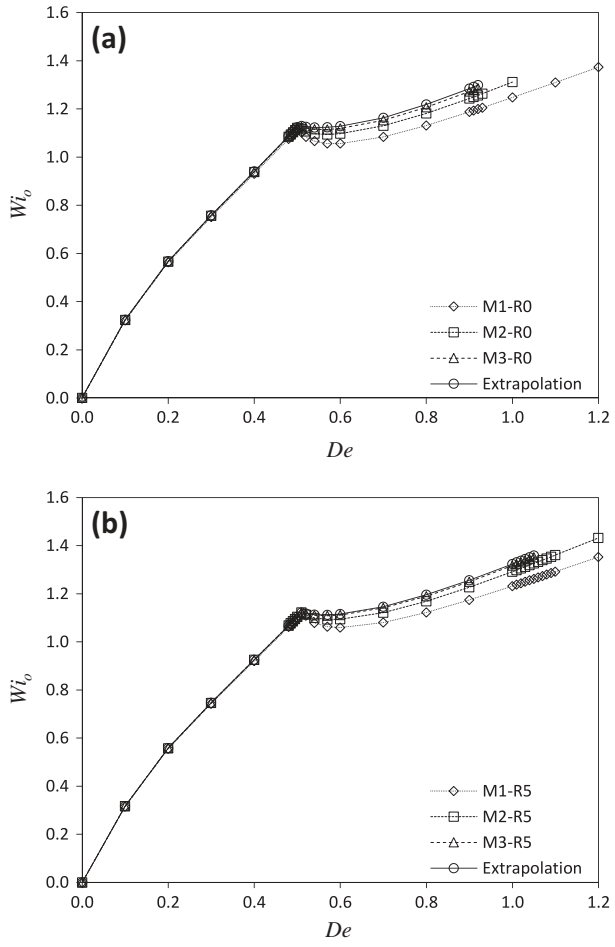

Fig. 4. Convergence with mesh refinement, for the sPTT model with $\beta = 1/9$ and $\varepsilon = 0.02$, of the Weissenberg number Wi_o as a function of De, calculated as the product of the relaxation time and strain rate at the stagnation point, $Wi_o = \lambda\dot{\varepsilon}_o$. M1, M2 and M3 are progressively finer meshes whose results converge towards the Richardson extrapolation limit with approximately second-order accuracy. Convergence is demonstrated for both the sharp corner (a) and rounded corner (b) meshes (see Table 1 for details). The curves are simply a guide to the eye.

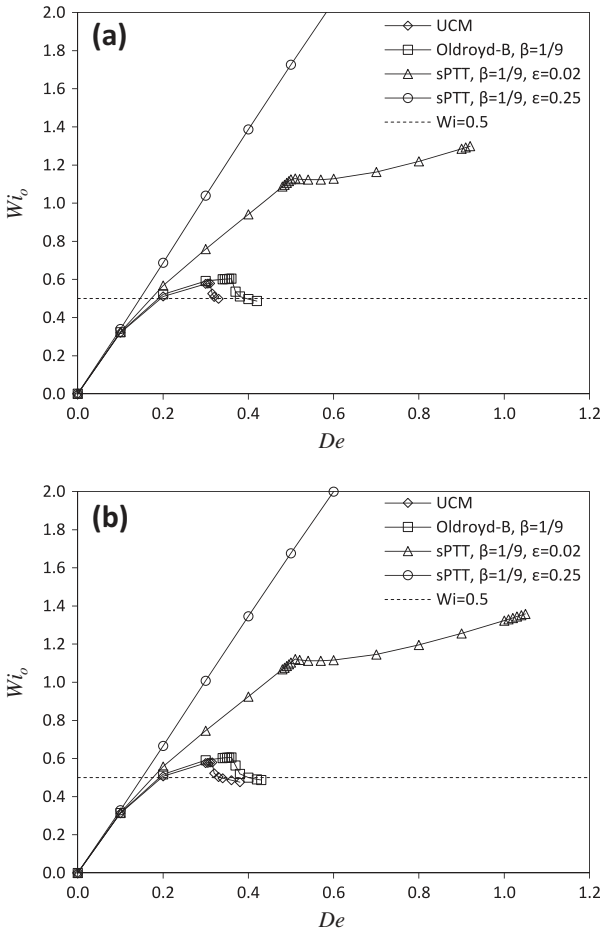

Fig. 5. Extrapolated values of the normalized strain rate at the stagnation point, Wi_o, as a function of De for all simulated models, $Wi_o = \lambda\dot{\varepsilon}_o$. Both the sharp corner (a) and rounded corner (b) geometries are represented (see Table 1 for details). The curves are simply a guide to the eye.

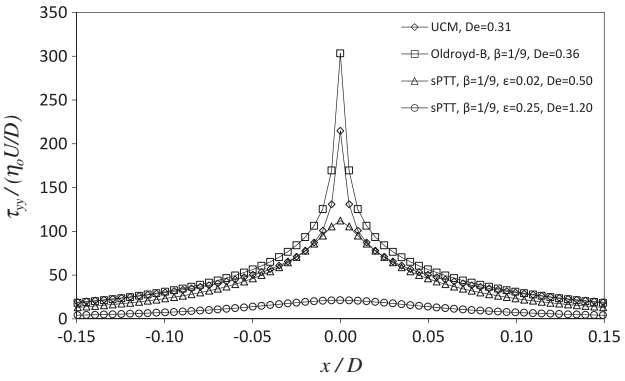

Fig. 6. Variation of the polymeric normalized normal stress τ_{yy} along the horizontal centreline ($y = 0$) for the highest De immediately prior to the transition to steady asymmetric flow or at the largest De simulated ($De = 1.20$) if no transition is observed. Data is provided for mesh M3-R0 (see Table 1 for details). The curves are simply a guide to the eye.

In the computational mesh the inlet and outlet arms are ten channel widths (D) in length for all fluid models (see Fig. 1(a)). Fully-developed velocity (average value U) and stress profiles are applied at the inlets and Neumann boundary conditions are assumed at the outlets for all variables including the pressure gradient. In the central square a uniform mesh with cell spacing $\Delta x_{\min} = \Delta y_{\min}$ is used, while in each arm the minimum cell spacing is the same as this minimum value in cells bordering the central square but becomes progressively larger away from this region. An odd number of cells across each arm, and in the central square, enables the calculation of the variables exactly along the centreline and at the stagnation point. Consistent mesh refinement, in which the minimum cell spacing is halved in each direction, was used to enable the computation of Richardson's extrapolation [33] for the asymmetry parameter DQ, Weissenberg number Wi_o at the cross-slot centre and Couette correction C. Considering three meshes with characteristic cell spacing h, $2h$ and $4h$, the order of convergence p for variable φ is given by [33]

$$p = \frac{\ln\left(\frac{\varphi_{2h}-\varphi_{4h}}{\varphi_h-\varphi_{2h}}\right)}{\ln 2}. \tag{4}$$

Given the order of convergence, the variable φ may be estimated for an infinitely refined mesh,

$$\varphi_0 = \frac{2^p\varphi_h - \varphi_{2h}}{2^p - 1}. \tag{5}$$

Table 1 documents the minimum cell spacing, total number of cells, degrees of freedom and corner radius of curvature for the six meshes used. The availability of data for rounded corners should allow the benchmarking of spectral or other higher-order computational methods, as well as a direct evaluation of the

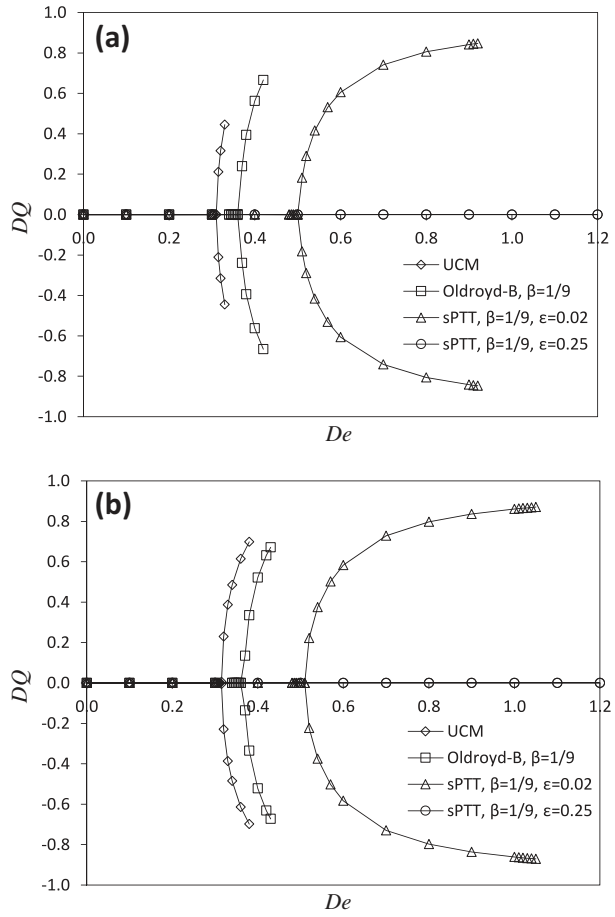

Fig. 7. Asymmetry parameter *DQ*, obtained by Richardson extrapolation, as a function of *De*, for both the sharp corner (a) and rounded corner (b) geometries (see Table 1 for details). Critical *De* values for both bifurcation and time-dependent flow are available in Table 2 and Table 3, respectively. No bifurcation is detected for the sPTT model with $\varepsilon = 0.25$ up to $De = 1.20$. The curves are simply a guide to the eye.

significance of cross-slot corners, and indeed wall boundary conditions, on the steady flow bifurcation. Furthermore, simulations were conducted at progressively higher *De*, and in smaller increments as the time-dependent flow range was approached, such that the critical Deborah number for the second transition could also be estimated accurately.

3. Numerical results and discussion

In Fig. 2(a)–(j) we plot the streamlines for some representative cases obtained using mesh M3-R0, where R0 denotes the geometry with sharp corners (see Table 1), superimposed upon contours of the dimensionless first normal-stress difference. The experimentally-observed asymmetry can be captured with the UCM, Oldroyd-B and sPTT models, at least if ε is sufficiently small (*cf.* Fig. 1 of [1] for experimental asymmetry patterns), as reported for geometrically-similar flow-focusing devices [18]. In Fig. 2 along each row the degree of elasticity increases from left to right. For the UCM model, the highest *De* which results in steady symmetric flow is represented in (a) at $De = 0.31$, along with the lowest *De* flow for steady asymmetry (b) at $De = 0.315$, followed by the highest *De* case prior to the onset of time-dependent flow (c) at $De = 0.33$. These three reference states are also represented for the Oldroyd-B model with $\beta = 1/9$, at (d) $De = 0.36$, (e) $De = 0.37$ and (f) $De = 0.42$ and the sPTT model with $\beta = 1/9$ and $\varepsilon = 0.02$, at (g) $De = 0.50$, (h) $De = 0.51$ and (i) $De = 0.92$. Between the second and third plot of each triplet, the flow becomes increasingly asymmetric. As implied in Fig. 2, the asymmetry may occur as either a clockwise or counter-clockwise rotation of the birefringence strand around the cross-slot centre, depending on numerical noise that induces the onset of flow asymmetry. Represented is also the (j) sPTT model with $\beta = 1/9$ and $\varepsilon = 0.25$ at $De = 1.20$, which remains steady and symmetric in the range of *De* tested – up to $De = 1.20$, with no hints of asymmetries or time-dependent flow. Fig. 3 provides contour maps of normalized velocity magnitude, relative pressure and extra-stress tensor component τ_{xy}, at $De = 0.36$ and $De = 0.42$, for the Oldroyd-B fluid.

Based on the numerical results it is possible to determine a local Weissenberg number, $Wi_o = \lambda\dot{\varepsilon}_o$, which we present as our first benchmark variable, calculated using the strain rate $\dot{\varepsilon}_o$ at the central stagnation point ($x = y = 0$),

$$\dot{\varepsilon}_o = \sqrt{\left(\frac{\partial u}{\partial x}\Big|_o\right)^2 + \frac{\partial u}{\partial y}\Big|_o \frac{\partial v}{\partial x}\Big|_o}. \tag{6}$$

In the vicinity of the stagnation point the 2D velocity field can, in general, be regarded as linear, and may thus be approximated as $[u, v] = [ax + by, cx - ay]$, with $a = (\partial u/\partial x)|_o = -(\partial v/\partial y)|_o$, $b = (\partial u/\partial y)|_o$ and $c = (\partial v/\partial x)|_o$. In matricial form the velocity field is written as $\mathbf{u} = \mathbf{A}\mathbf{x}$. The positive eigenvalue of this linear transformation provides the extensional strain rate given by Eq. (6), while the corresponding eigenvectors represent the principal axes defined by the streamlines that cross the stagnation point, which are not normal to each other in an asymmetric steady flow scenario. For symmetric flow the strain rate at the stagnation point simplifies to $\dot{\varepsilon}_o = -(\partial u/\partial x)|_o = (\partial v/\partial y)|_o$.

In Fig. 4 we demonstrate the mesh-wise convergence and Richardson extrapolation of *Wi* at the stagnation point for the sPTT model with $\varepsilon = 0.02$, for both the sharp and rounded corner configurations, while in Fig. 5 we present extrapolated results for all models and geometries. From the numerical data of Wi_o we computed an average order of convergence of 2.2, which follows closely the expected second-order accuracy of the numerical method. Notably for both the UCM and Oldroyd-B models the local Weissenberg number at the stagnation point exceeds the theoretical critical value of 1/2. Therefore, at this point, the extensional stresses can become unbounded, since the residence time is infinitely large – for the sPTT model, for which the normal stresses are bounded, this concern is not an issue. Steady-state solutions can still be obtained because at the stagnation point, although singular, the stresses remain integrable (see the interesting discussion in Rallison and Hinch [34]). That the stresses become unbounded well below the critical *De* for asymmetric flow, in conjunction with the fact that the asymmetry is also observed for the sPTT model, shows the asymmetry is not directly related to this local stress singularity. Rocha et al. [15] examined the influence of finite extensi-

Table 2
Square root fit, $DQ = A\sqrt{De - De_{CR}}$, for *De* above the first critical value. The first three points after bifurcation (see Fig. 7) were fitted and the minimization of the sum of point-wise relative error was used as objective function. S_r is the point-wise average relative error. *Rounded* refers to meshes whose corners have been rounded to a radius of curvature of 5% of the channels' width.

Model	Corner	A	De_{CR}	S_r
UCM	Sharp	3.20	0.311	0.6%
Oldroyd-B, $\beta = 1/9$	Sharp	2.94	0.363	1.3%
sPTT, $\beta = 1/9$, $\varepsilon = 0.02$	Sharp	2.16	0.503	0.9%
sPTT, $\beta = 1/9$, $\varepsilon = 0.25$	Sharp	No bifurcation up to $De = 1.20$		
UCM	Rounded	3.20	0.315	2.4%
Oldroyd-B, $\beta = 1/9$	Rounded	2.91	0.368	1.5%
sPTT, $\beta = 1/9$, $\varepsilon = 0.02$	Rounded	2.01	0.508	1.2%
sPTT, $\beta = 1/9$, $\varepsilon = 0.25$	Rounded	No bifurcation up to $De = 1.20$		

Table 3
Estimated values of *De* for the second critical transition, from steady asymmetric flow to time-dependent behaviour, obtained from the more refined meshes, M3-R0 and M3-R5. *Rounded* refers to the M3-R5 meshes, whose corners have been rounded to a radius of curvature of 5% of the channel width.

Model	Corner	Highest steady *De*	Lowest unsteady *De*	Estimated critical *De*
UCM	Sharp	0.330	0.340	0.335
Oldroyd-B, $\beta = 1/9$	Sharp	0.420	0.430	0.425
sPTT, $\beta = 1/9$, $\varepsilon = 0.02$	Sharp	0.920	0.930	0.925
sPTT, $\beta = 1/9$, $\varepsilon = 0.25$	Sharp	Steady flow up to $De = 1.20$		
UCM	Rounded	0.380	0.390	0.385
Oldroyd-B, $\beta = 1/9$	Rounded	0.430	0.440	0.435
sPTT, $\beta = 1/9$, $\varepsilon = 0.02$	Rounded	1.050	1.060	1.055
sPTT, $\beta = 1/9$, $\varepsilon = 0.25$	Rounded	Steady flow up to $De = 1.20$		

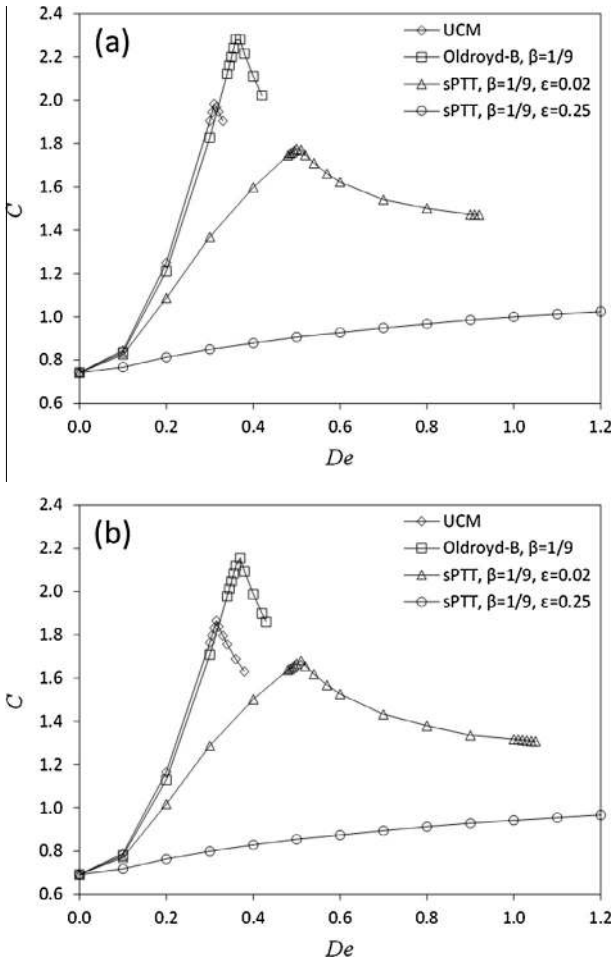

Fig. 8. Couette correction *C*, obtained by Richardson extrapolation, as a function of *De*. At the onset of steady asymmetric flow the Couette correction decreases, indicating a relative decrease in flow resistance. Data is provided for both the sharp corner (a) and rounded corner (b) geometries (see Table 1 for details). The curves are simply a guide to the eye.

bility upon the bifurcation phenomenon and concluded that, even though higher extensibility promotes steady asymmetries at lower *De*, infinite extensibility such as in the UCM and Oldroyd-B models is not a necessary condition for steady symmetry breaking. In Fig. 6 we plot the variation of the polymeric component of stress τ_{yy} along the horizontal (upstream) centreline for mesh M3-R0 (see Table 1), demonstrating the asymptotically singular nature of the UCM and Oldroyd-B models near the stagnation point. We emphasize that at such flow conditions ($Wi_0 > 0.5$), the normal stress τ_{yy} is unbounded in the region along the outlet centreline for both the UCM and the Oldroyd-B models. Thus, there is a local loss of accuracy near the stagnation point in the numerical solution, which predicts a very large, yet bounded normal stress. This loss of accuracy is limited to a narrow region near the stagnation point, and therefore is not of significant concern. Further mesh refinement would lead to an increase of τ_{yy} in the vicinity of the cross-slot centre, with $\tau_{yy,o} \to \infty$ for cell spacing $\Delta x_{\min}$, $\Delta y_{\min} \to 0$, for the UCM and Oldroyd-B models.

Although the streamline plots of Fig. 2 provide a qualitative visual indication of the degree of flow asymmetry, a suitable quantitative parameter is necessary as a reliable benchmark variable. An intuitive measure of the degree of asymmetry is the relative split of flow from an inlet arm heading towards each outlet arm, which in a symmetric flow would be 50%. A suitable scalar is the flow asymmetry parameter, proposed by Poole et al. [3]:

$$DQ = \frac{q_2 - q_1}{q_1 + q_2}. \tag{7}$$

The total flow rate per unit depth supplied to each inlet channel, $Q = UD = q_1 + q_2$, divides into two outlet streams. For instance, for the west inlet arm, as illustrated in Fig. 1(a), the total flow divides into the north outflow arm, q_1 plus the south outflow arm, q_2. For a symmetric flow $DQ = 0$ and for a completely asymmetric flow $|DQ| = 1$, *i.e.* flow from one inlet channel going completely to a single outlet channel. We stress that the total flow rate Q leaving each outlet arm remains unaltered in both the symmetric and asymmetric states, since the latter has an anti-symmetric nature. The Richardson extrapolation of this asymmetry parameter as a function of *De* is provided in Fig. 7, for both sharp and rounded corners. The average order of convergence for *DQ* is 2.1, in agreement with the second-order accuracy of the numerical method used. In order to accurately determine the critical conditions of flow transition, De_{CR}, we fitted the first three points post-bifurcation with the expected square-root formula for supercritical pitchfork bifurcations, $DQ = A\sqrt{De - De_{CR}}$, where A is a scale factor and De_{CR} is the critical transition *De*. We opted for a square-root fit over a general curve fit because the data follows the usual trend of a supercritical pitchfork bifurcation, as also pointed out by Wilson [24]. The fit was not extended to higher *De* since pitchfork bifurcations are intrinsically local (note the lines in Fig. 7 are just data point connections used as visual aids). Fitted parameters and error are given in Table 2. As expected from previous work [15], the influence of corner sharpness is negligible upon the critical *De* for onset of steady asymmetric flow.

As for the second critical Deborah number, which governs the transition to time-dependent flow, we used an approximate method based on the determination of the highest steady *De* and lowest unsteady *De* flows for each fluid, using data obtained from the finer meshes available, M3-R0 and M3-R5 (see Table 1 for details). Using steps of 0.01 for *De*, we were thus able to determine the second critical *De* with an absolute error of ±0.005. As seen in Table 3, a radius of curvature of only 5% of the channel width is sufficient to significantly delay the onset of time-dependent flow for the UCM and sPTT (at $\varepsilon = 0.02$) models to higher *De* values. This indicates a distinct source for the two

Table 4
UCM model data for a cross-slot with sharp corners. Osc stands for oscillatory flow.

De	$Wi_o = \lambda\dot{\varepsilon}_o$				$\lvert DQ\rvert$				C			
	M1	M2	M3	Extrap.	M1	M2	M3	Extrap.	M1	M2	M3	Extrap.
0.000	0.000	0.000	0.000	0.000	0.000	0.000	0.000	0.000	0.733	0.738	0.741	0.743
0.100	0.318	0.319	0.320	0.320	0.000	0.000	0.000	0.000	0.831	0.839	0.842	0.845
0.200	0.507	0.509	0.511	0.511	0.000	0.000	0.000	0.000	1.232	1.245	1.247	1.249
0.300	0.571	0.574	0.575	0.576	0.000	0.000	0.000	0.000	1.905	1.911	1.908	1.906
0.305	0.572	0.576	0.577	0.577	0.000	0.000	0.000	0.000	1.944	1.949	1.946	1.944
0.310	0.574	0.577	0.578	0.579	0.000	0.000	0.000	0.000	1.984	1.988	1.985	1.983
0.315	0.552	0.535	0.528	0.526	0.138	0.203	0.209	0.211	1.994	1.976	1.972	1.969
0.320	0.529	0.515	0.511	0.509	0.270	0.312	0.315	0.315	1.972	1.951	1.949	1.947
0.330	0.509	0.502	0.500	0.499	0.415	0.441	0.444	0.445	1.929	1.910	1.908	1.905
0.340	0.499	0.494	Osc.	–	0.508	0.527	Osc.	–	1.893	1.875	Osc.	–
0.360	0.485	0.481	Osc.	–	0.631	0.646	Osc.	–	1.831	1.816	Osc.	–
0.380	0.472	0.468	Osc.	–	0.712	0.724	Osc.	–	1.781	1.767	Osc.	–
0.400	0.460	0.456	Osc.	–	0.770	0.780	Osc.	–	1.741	1.729	Osc.	–
0.500	0.407	Osc.	Osc.	–	0.907	Osc.	Osc.	–	1.643	Osc.	Osc.	–
0.600	Osc.	Osc.	Osc.	–	Osc.	Osc.	Osc.	–	Osc.	Osc.	Osc.	–

Table 5
Oldroyd-B model data, with $\beta = 1/9$, for a cross-slot with sharp corners. Osc stands for oscillatory flow.

De	$Wi_o = \lambda\dot{\varepsilon}_o$				$\lvert DQ\rvert$				C			
	M1	M2	M3	Extrap.	M1	M2	M3	Extrap.	M1	M2	M3	Extrap.
0.000	0.000	0.000	0.000	0.000	0.000	0.000	0.000	0.000	0.733	0.738	0.741	0.743
0.100	0.320	0.321	0.322	0.322	0.000	0.000	0.000	0.000	0.822	0.829	0.833	0.835
0.200	0.519	0.521	0.522	0.522	0.000	0.000	0.000	0.000	1.195	1.207	1.209	1.211
0.300	0.588	0.590	0.591	0.591	0.000	0.000	0.000	0.000	1.830	1.836	1.832	1.828
0.340	0.598	0.600	0.600	0.600	0.000	0.000	0.000	0.000	2.135	2.134	2.128	2.123
0.345	0.599	0.601	0.601	0.601	0.000	0.000	0.000	0.000	2.175	2.173	2.167	2.162
0.350	0.600	0.602	0.602	0.602	0.000	0.000	0.000	0.000	2.215	2.212	2.206	2.201
0.355	0.600	0.602	0.602	0.602	0.001	0.000	0.000	0.000	2.255	2.252	2.246	2.241
0.360	0.601	0.602	0.603	0.603	0.002	0.007	0.000	0.000	2.296	2.291	2.286	2.282
0.370	0.561	0.543	0.538	0.537	0.221	0.260	0.244	0.239	2.291	2.264	2.274	2.281
0.380	0.530	0.518	0.512	0.511	0.381	0.401	0.396	0.394	2.226	2.206	2.211	2.215
0.400	0.507	0.500	0.498	0.497	0.550	0.563	0.563	0.562	2.124	2.107	2.109	2.111
0.420	0.493	0.488	0.487	0.487	0.653	0.664	0.665	0.666	2.038	2.026	2.024	2.023
0.430	0.486	0.482	Osc.	–	0.692	0.702	Osc.	–	2.002	1.991	Osc.	–
0.500	0.445	Osc.	Osc.	–	0.850	Osc.	Osc.	–	1.823	Osc.	Osc.	–
0.600	0.390	Osc.	Osc.	–	0.934	Osc.	Osc.	–	1.720	Osc.	Osc.	–
0.700	Osc.	Osc.	Osc.	–	Osc.	Osc.	Osc.	–	Osc.	Osc.	Osc.	–

Table 6
sPTT model data, with $\beta = 1/9$ and $\varepsilon = 0.02$, for a cross-slot with sharp corners. Osc stands for oscillatory flow.

De	$Wi_o = \lambda\dot{\varepsilon}_o$				$\lvert DQ\rvert$				C			
	M1	M2	M3	Extrap.	M1	M2	M3	Extrap.	M1	M2	M3	Extrap.
0.000	0.000	0.000	0.000	0.000	0.000	0.000	0.000	0.000	0.733	0.738	0.741	0.743
0.100	0.322	0.324	0.324	0.324	0.000	0.000	0.000	0.000	0.812	0.819	0.822	0.825
0.200	0.563	0.566	0.567	0.568	0.000	0.000	0.000	0.000	1.075	1.084	1.085	1.087
0.300	0.751	0.756	0.758	0.758	0.000	0.000	0.000	0.000	1.372	1.374	1.372	1.370
0.400	0.931	0.938	0.940	0.940	0.000	0.000	0.000	0.000	1.619	1.611	1.604	1.598
0.480	1.075	1.084	1.086	1.087	0.000	0.000	0.000	0.000	1.774	1.761	1.753	1.746
0.485	1.084	1.094	1.096	1.096	0.000	0.000	0.000	0.000	1.783	1.769	1.761	1.755
0.490	1.093	1.103	1.105	1.105	0.001	0.001	0.000	0.000	1.792	1.778	1.768	1.760
0.495	1.102	1.112	1.114	1.115	0.001	0.001	0.001	0.001	1.801	1.786	1.776	1.768
0.500	1.111	1.121	1.123	1.124	0.001	0.003	0.001	0.001	1.809	1.795	1.784	1.776
0.510	1.102	1.115	1.125	1.128	0.173	0.194	0.184	0.181	1.804	1.784	1.777	1.772
0.520	1.084	1.106	1.120	1.124	0.282	0.295	0.291	0.290	1.784	1.764	1.755	1.747
0.540	1.066	1.097	1.115	1.120	0.405	0.417	0.417	0.416	1.746	1.727	1.717	1.710
0.570	1.057	1.094	1.115	1.121	0.518	0.530	0.531	0.531	1.698	1.681	1.670	1.661
0.600	1.057	1.097	1.119	1.125	0.593	0.604	0.606	0.606	1.663	1.645	1.633	1.623
0.700	1.084	1.130	1.153	1.160	0.727	0.738	0.741	0.742	1.590	1.567	1.552	1.541
0.800	1.131	1.181	1.207	1.215	0.791	0.802	0.805	0.806	1.556	1.528	1.513	1.501
0.900	1.187	1.243	1.272	1.280	0.828	0.838	0.841	0.842	1.527	1.504	1.487	1.473
0.910	1.193	1.250	1.279	1.287	0.831	0.841	0.844	0.845	1.526	1.503	1.486	1.473
0.920	1.199	1.256	1.286	1.294	0.834	0.844	0.847	0.847	1.549	1.501	1.485	1.472
0.930	1.205	1.263	Osc.	–	0.836	0.846	Osc.	–	1.538	1.504	Osc.	–
1.000	1.248	1.311	Osc.	–	0.852	0.861	Osc.	–	1.523	1.495	Osc.	–
1.100	1.310	Osc.	Osc.	–	0.868	Osc.	Osc.	–	1.534	Osc.	Osc.	–
1.200	1.373	Osc.	Osc.	–	0.879	Osc.	Osc.	–	1.548	Osc.	Osc.	–

Table 7
sPTT model data, with $\beta = 1/9$ and $\varepsilon = 0.25$, for a cross-slot with sharp corners.

De	$Wi_o = \lambda\dot{\varepsilon}_o$				$\lvert DQ\rvert$				C			
	M1	M2	M3	Extrap.	M1	M2	M3	Extrap.	M1	M2	M3	Extrap.
0.000	0.000	0.000	0.000	0.000	0.000	0.000	0.000	0.000	0.733	0.738	0.741	0.743
0.100	0.337	0.338	0.339	0.339	0.000	0.000	0.000	0.000	0.757	0.762	0.765	0.767
0.200	0.681	0.685	0.686	0.687	0.000	0.000	0.000	0.000	0.803	0.808	0.811	0.813
0.300	1.030	1.036	1.038	1.038	0.000	0.000	0.000	0.000	0.840	0.846	0.848	0.850
0.400	1.375	1.383	1.385	1.386	0.000	0.000	0.000	0.000	0.877	0.878	0.879	0.880
0.500	1.712	1.722	1.725	1.726	0.000	0.000	0.000	0.000	0.900	0.905	0.906	0.906
0.600	2.040	2.052	2.056	2.057	0.000	0.000	0.000	0.000	0.927	0.930	0.929	0.927
0.700	2.361	2.375	2.379	2.380	0.000	0.000	0.000	0.000	0.948	0.949	0.949	0.949
0.800	2.674	2.690	2.695	2.696	0.000	0.000	0.000	0.000	0.966	0.968	0.968	0.967
0.900	2.982	3.000	3.005	3.006	0.000	0.000	0.000	0.000	0.985	0.986	0.985	0.985
1.000	3.284	3.304	3.309	3.311	0.000	0.000	0.000	0.000	1.001	1.000	1.000	0.999
1.100	3.581	3.603	3.610	3.611	0.000	0.000	0.000	0.000	1.014	1.014	1.013	1.012
1.200	3.874	3.899	3.906	3.908	0.000	0.000	0.000	0.000	1.027	1.026	1.025	1.024

Table 8
UCM model data for a cross-slot with rounded corners with a radius of curvature equal to 5% of the channel width. Osc stands for oscillatory flow.

De	$Wi_o = \lambda\dot{\varepsilon}_o$				$\lvert DQ\rvert$				C			
	M1	M2	M3	Extrap.	M1	M2	M3	Extrap.	M1	M2	M3	Extrap.
0.000	0.000	0.000	0.000	0.000	0.000	0.000	0.000	0.000	0.694	0.695	0.693	0.692
0.100	0.312	0.313	0.313	0.313	0.000	0.000	0.000	0.000	0.789	0.791	0.791	0.790
0.200	0.504	0.506	0.506	0.506	0.000	0.000	0.000	0.000	1.173	1.173	1.169	1.166
0.300	0.571	0.575	0.576	0.576	0.000	0.000	0.000	0.000	1.818	1.797	1.779	1.765
0.305	0.573	0.576	0.577	0.578	0.000	0.000	0.000	0.000	1.855	1.833	1.814	1.798
0.310	0.574	0.578	0.579	0.579	0.000	0.000	0.000	0.000	1.893	1.869	1.848	1.832
0.315	0.576	0.579	0.580	0.580	0.000	0.002	0.004	0.005	1.931	1.906	1.883	1.865
0.320	0.554	0.537	0.526	0.523	0.132	0.199	0.221	0.228	1.943	1.892	1.861	1.837
0.330	0.517	0.508	0.504	0.503	0.351	0.377	0.384	0.387	1.897	1.847	1.818	1.796
0.340	0.504	0.499	0.497	0.496	0.463	0.480	0.484	0.485	1.857	1.807	1.779	1.756
0.360	0.489	0.486	0.486	0.486	0.603	0.612	0.614	0.614	1.790	1.740	1.711	1.688
0.380	0.476	0.474	0.476	0.476	0.691	0.698	0.698	0.698	1.737	1.686	1.655	1.630
0.390	0.471	0.469	Osc.	–	0.725	0.730	Osc.	–	1.713	1.663	Osc.	–
0.400	0.465	0.463	Osc.	–	0.754	0.758	Osc.	–	1.692	1.641	Osc.	–
0.500	0.414	Osc.	Osc.	–	0.898	Osc.	Osc.	–	1.572	Osc.	Osc.	–
0.600	0.378	Osc.	Osc.	–	0.947	Osc.	Osc.	–	1.540	Osc.	Osc.	–
0.700	Osc.	Osc.	Osc.	–	Osc.	Osc.	Osc.	–	Osc.	Osc.	Osc.	–

Table 9
Oldroyd-B model data, with $\beta = 1/9$, for a cross-slot with rounded corners with a radius of curvature equal to 5% of the channel width. Osc stands for oscillatory flow.

De	$Wi_o = \lambda\dot{\varepsilon}_o$				$\lvert DQ\rvert$				C			
	M1	M2	M3	Extrap.	M1	M2	M3	Extrap.	M1	M2	M3	Extrap.
0.000	0.000	0.000	0.000	0.000	0.000	0.000	0.000	0.000	0.694	0.695	0.693	0.692
0.100	0.314	0.314	0.315	0.315	0.000	0.000	0.000	0.000	0.779	0.781	0.781	0.781
0.200	0.515	0.517	0.517	0.517	0.000	0.000	0.000	0.000	1.134	1.135	1.132	1.130
0.300	0.589	0.591	0.591	0.591	0.000	0.000	0.000	0.000	1.738	1.727	1.716	1.708
0.340	0.600	0.602	0.602	0.602	0.000	0.000	0.000	0.000	2.029	2.008	1.991	1.977
0.345	0.601	0.603	0.603	0.603	0.000	0.000	0.000	0.000	2.066	2.044	2.026	2.012
0.350	0.602	0.604	0.604	0.604	0.000	0.000	0.000	0.000	2.104	2.081	2.062	2.047
0.355	0.603	0.605	0.605	0.605	0.000	0.000	0.000	0.000	2.143	2.118	2.098	2.082
0.360	0.603	0.605	0.606	0.606	0.000	0.000	0.000	0.000	2.182	2.155	2.134	2.118
0.370	0.590	0.578	0.566	0.563	0.063	0.090	0.123	0.133	2.244	2.209	2.178	2.154
0.380	0.549	0.531	0.521	0.519	0.289	0.321	0.331	0.335	2.199	2.147	2.117	2.093
0.400	0.514	0.506	0.501	0.500	0.500	0.514	0.519	0.521	2.089	2.042	2.011	1.987
0.420	0.499	0.493	0.492	0.491	0.619	0.627	0.630	0.631	1.998	1.952	1.922	1.899
0.430	0.492	0.488	0.487	0.487	0.662	0.669	0.671	0.672	1.958	1.913	1.883	1.860
0.440	0.486	0.483	Osc.	–	0.699	0.705	Osc.	–	1.922	1.877	Osc.	–
0.500	0.452	0.449	Osc.	–	0.835	0.838	Osc.	–	1.761	1.711	Osc.	–
0.600	0.401	0.392	Osc.	–	0.925	0.927	Osc.	–	1.625	1.564	Osc.	–
0.700	Osc.	Osc.	Osc.	–	Osc.	Osc.	Osc.	–	Osc.	Osc.	Osc.	–

transitions in the cross-slot system: the steady bifurcation occurs as a result of large normal stresses and gradients in the birefringence strand, while the unsteady flow transition seems to result from instabilities generated along curved streamlines near the corners, as predicted by the Larson micromechanical model [16], which are quantifiable using the Pakdel–McKinley criterion [17]. However, for the Oldroyd-B model, only a small increase in the second critical De was observed for the rounded corner simulations (see Table 3), and presently we are unable to explain this apparent inconsistency.

Table 10
sPTT model data, with $\beta = 1/9$ and $\varepsilon = 0.02$, for a cross-slot with rounded corners with a radius of curvature equal to 5% of the channel width. Osc stands for oscillatory flow.

De	$Wi_o = \lambda\dot{\varepsilon}_o$				$\lvert DQ\rvert$				C			
	M1	M2	M3	Extrap.	M1	M2	M3	Extrap.	M1	M2	M3	Extrap.
0.000	0.000	0.000	0.000	0.000	0.000	0.000	0.000	0.000	0.694	0.695	0.693	0.692
0.100	0.316	0.316	0.317	0.317	0.000	0.000	0.000	0.000	0.770	0.772	0.772	0.772
0.200	0.556	0.558	0.558	0.558	0.000	0.000	0.000	0.000	1.022	1.023	1.020	1.017
0.300	0.743	0.746	0.746	0.746	0.000	0.000	0.000	0.000	1.308	1.302	1.294	1.287
0.400	0.920	0.925	0.925	0.925	0.000	0.000	0.000	0.000	1.545	1.528	1.513	1.502
0.480	1.062	1.068	1.068	1.068	0.000	0.000	0.000	0.000	1.698	1.671	1.652	1.637
0.485	1.071	1.077	1.077	1.077	0.000	0.000	0.000	0.000	1.707	1.679	1.658	1.642
0.490	1.080	1.086	1.086	1.086	0.000	0.000	0.000	0.000	1.715	1.687	1.666	1.650
0.495	1.089	1.095	1.095	1.095	0.000	0.000	0.000	0.000	1.723	1.694	1.673	1.657
0.500	1.098	1.104	1.104	1.104	0.000	0.000	0.000	0.000	1.732	1.702	1.682	1.667
0.510	1.115	1.122	1.122	1.121	0.000	0.000	0.000	0.000	1.748	1.717	1.697	1.681
0.520	1.109	1.113	1.116	1.117	0.157	0.202	0.217	0.221	1.747	1.703	1.677	1.656
0.540	1.079	1.099	1.110	1.113	0.342	0.364	0.372	0.374	1.707	1.664	1.638	1.618
0.570	1.063	1.093	1.108	1.113	0.478	0.495	0.500	0.501	1.658	1.614	1.588	1.568
0.600	1.059	1.094	1.111	1.116	0.563	0.578	0.582	0.583	1.620	1.574	1.547	1.527
0.700	1.080	1.121	1.141	1.147	0.713	0.724	0.728	0.729	1.530	1.485	1.456	1.433
0.800	1.122	1.169	1.190	1.196	0.783	0.793	0.796	0.797	1.484	1.436	1.405	1.380
0.900	1.174	1.227	1.250	1.257	0.822	0.832	0.835	0.836	1.462	1.408	1.368	1.336
1.000	1.232	1.292	1.317	1.324	0.847	0.857	0.860	0.861	1.453	1.388	1.348	1.317
1.010	1.238	1.298	1.324	1.331	0.849	0.859	0.862	0.863	1.452	1.386	1.347	1.316
1.020	1.244	1.305	1.331	1.338	0.851	0.860	0.864	0.865	1.451	1.385	1.345	1.314
1.030	1.250	1.312	1.338	1.345	0.853	0.862	0.866	0.867	1.434	1.384	1.343	1.312
1.040	1.256	1.319	1.345	1.352	0.855	0.864	0.867	0.868	1.433	1.383	1.342	1.310
1.050	1.262	1.326	1.352	1.359	0.857	0.866	0.869	0.870	1.432	1.382	1.341	1.308
1.060	1.268	1.333	Osc.	–	0.858	0.867	Osc.	–	1.445	1.382	Osc.	–
1.070	1.274	1.340	Osc.	–	0.860	0.869	Osc.	–	1.445	1.382	Osc.	–
1.080	1.280	1.347	Osc.	–	0.861	0.871	Osc.	–	1.444	1.381	Osc.	–
1.090	1.286	1.354	Osc.	–	0.863	0.872	Osc.	–	1.433	1.380	Osc.	–
1.100	1.292	1.361	Osc.	–	0.864	0.873	Osc.	–	1.435	1.379	Osc.	–
1.200	1.353	1.432	Osc.	–	0.877	0.886	Osc.	–	1.440	1.377	Osc.	–

Table 11
sPTT model data, with $\beta = 1/9$ and $\varepsilon = 0.25$, for a cross-slot with rounded corners with a radius of curvature equal to 5% of the channel width.

De	$Wi_o = \lambda\dot{\varepsilon}_o$				$\lvert DQ\rvert$				C			
	M1	M2	M3	Extrap.	M1	M2	M3	Extrap.	M1	M2	M3	Extrap.
0.000	0.000	0.000	0.000	0.000	0.000	0.000	0.000	0.000	0.694	0.695	0.693	0.692
0.100	0.328	0.329	0.329	0.329	0.000	0.000	0.000	0.000	0.718	0.720	0.719	0.719
0.200	0.664	0.666	0.666	0.666	0.000	0.000	0.000	0.000	0.765	0.766	0.765	0.764
0.300	1.005	1.008	1.008	1.008	0.000	0.000	0.000	0.000	0.804	0.803	0.802	0.800
0.400	1.343	1.346	1.346	1.346	0.000	0.000	0.000	0.000	0.834	0.833	0.831	0.829
0.500	1.673	1.677	1.677	1.677	0.000	0.000	0.000	0.000	0.863	0.859	0.857	0.855
0.600	1.995	2.000	2.000	2.000	0.000	0.000	0.000	0.000	0.886	0.883	0.878	0.874
0.700	2.309	2.316	2.315	2.315	0.000	0.000	0.000	0.000	0.905	0.901	0.898	0.895
0.800	2.616	2.624	2.623	2.623	0.000	0.000	0.000	0.000	0.923	0.920	0.916	0.913
0.900	2.917	2.926	2.925	2.925	0.000	0.000	0.000	0.000	0.941	0.936	0.932	0.930
1.000	3.213	3.223	3.223	3.222	0.000	0.000	0.000	0.000	0.956	0.950	0.946	0.943
1.100	3.504	3.516	3.515	3.515	0.000	0.000	0.000	0.000	0.969	0.962	0.959	0.956
1.200	3.791	3.805	3.804	3.804	0.000	0.000	0.000	0.000	0.981	0.974	0.970	0.967

Although there are a number of possible ways to quantify the additional pressure drop that arises due to the strong extensional flow within the cross-slot, we choose here to use the Couette correction, our third benchmark variable, defined as

$$C \equiv \frac{\Delta p - \Delta p_{fd}}{2\tau_w}, \tag{8}$$

where Δp is the overall pressure drop between two points located far away from the central region – one upstream and one downstream – under fully developed flow conditions, including the cross slot central region; τ_w is the total wall shear stress, (solvent plus polymer contributions), in fully-developed channel flows; and Δp_{fd} is the pressure-drop required to drive that same fully-developed flow in a straight channel, in the absence of the slot, *i.e.* simple-shear flow between the two points chosen to determine Δp, not accounting for the length of the central square. Thus one may think of the Couette correction as the number of channel widths the planar channel would have to be extended by to produce the same pressure drop induced by the presence of the cross-slot. Note that $2\tau_w = |dp/dx|_{fd}\ D = |dp/dy|_{fd}\ D$. The variation of this measure of the additional pressure drop with De is shown in Fig. 8 for both geometries. The obtained average order of convergence for C is 1.2, somewhat lower than the expected value for a second-order method, because additional errors are introduced in the calculation procedure for C, namely the extrapolation used to determine the fully developed pressure drop and the difference between two small quantities. Upon bifurcation the viscoelastic fluid dissipates significantly less energy as it flows through the cross slot than it would if it did so flowing symmetrically at the same De, in agreement with previous results for both 2D [3,15] and uniaxial extension in 3D [20] cross-slot simulations. For the sPTT model with $\varepsilon = 0.25$, for which no bifurcation was observed up to $De = 1.20$, the sudden decrease in Couette correction is not observed. Also, as expected, rounding

the cross-slot corners generally slightly decreases the pressure drop necessary to drive flow.

In the spirit of this benchmark-proposing paper, all previously discussed data is provided in detail in tabular form. For sharp corner geometries, Tables 4 and 5 include data on the three benchmark parameters – Wi_o, DQ and C – for the UCM and Oldroyd-B models, respectively, while Tables 6 and 7 provide the same data for the sPTT model, with $\varepsilon = 0.02$ and $\varepsilon = 0.25$, respectively. Similarly, data for rounded corners is given in Tables 8 and 9 for the UCM and Oldroyd-B models, respectively, while data for the sPTT model, with $\varepsilon = 0.02$ and $\varepsilon = 0.25$, can be found in Table 10 and Table 11, respectively. Furthermore, as discussed, the critical values of De for the first and second flow transitions are listed in Table 2 and Table 3, respectively.

4. Conclusions

We provide detailed numerical data of flow quantities of interest for three different viscoelastic models in the cross-slot geometry, with particular emphasis placed on the bifurcation to steady asymmetric flow which occurs at a critical Deborah number. We propose that this steady flow bifurcation – in such a conceptually simple geometry – makes an excellent test case against which to benchmark, and compare, different numerical schemes for the simulation of viscoelastic fluid flows and have accordingly provided numerical data. We also estimate the critical De for the onset of time-dependent flow. We provide data for the standard sharp corner cross-slot and also for a slightly rounded geometry, so that benchmarking of spectral or other higher-order methods is not impeded by the existence of geometrical singularities due to sharp corners. The proposed benchmark variables – local Weissenberg number Wi_o at the stagnation point, asymmetry parameter DQ, Couette correction C, and the critical De values – can also be measured experimentally, offering a standardized form of communicating results for the cross slot flow. The occurrence of an interior stagnation point, away from any boundary conditions, where the stress field can become unbounded is also a noteworthy flow feature, useful for benchmarking of numerical simulations.

Acknowledgments

F.A. Cruz and M.A. Alves acknowledge funding from the European Research Council (ERC), under the European Commission "Ideas" specific programme of the 7th Framework Programme, Grant Agreement N° 307499. A.M. Afonso would also like to thank Fundação para a Ciência e a Tecnologia for financial support through the scholarship SFRH/BPD/75436/2010.

References

[1] P.E. Arratia, C.C. Thomas, J. Diorio, J.P. Gollub, Elastic instabilities of polymer solutions in cross-channel flow, Phys. Rev. Lett. 96 (2006) 144502, http://dx.doi.org/10.1103/PhysRevLett. 96.144502.
[2] K. Gardner, E. Pike, M. Miles, A. Keller, K. Tanaka, Photon-correlation velocimetry of polystyrene solutions in extensional flow fields, Polymer 23 (1982) 1435–1442, http://dx.doi.org/10.1016/0032-3861(82)90240-3.
[3] R.J. Poole, M.A. Alves, P.J. Oliveira, Purely elastic flow asymmetries, Phys. Rev. Lett. 99 (2007) 164503, http://dx.doi.org/10.1103/PhysRevLett. 99.164503.
[4] G.I. Taylor, Stability of a viscous liquid contained between two rotating cylinders, Philos. Trans. Roy. Soc. A: Math. Phys. Eng. Sci. 223 (1923) 289–343, http://dx.doi.org/10.1098/rsta.1923.0008.
[5] J.G. Oldroyd, On the formulation of rheological equations of state, Proc. Roy. Soc. A: Math. Phys. Eng. Sci. 200 (1950) 523–541, http://dx.doi.org/10.1098/rspa.1950.0035.
[6] N. Phan-Thien, R.I. Tanner, A new constitutive equation derived from network theory, J. Non-Newt. Fluid Mech. 2 (1977) 353–365, http://dx.doi.org/10.1016/0377-0257(77)80021-9.
[7] J.F.M. Schoonen, F.H.M. Swartjes, G.W.M. Peters, F.P.T. Baaijens, H.E.H. Meijer, A 3D numerical/experimental study on a stagnation flow of a polyisobutylene solution, J. Non-Newt. Fluid Mech. 79 (1998) 529–561, http://dx.doi.org/10.1016/S0377-0257(98)00118-9.
[8] J. Remmelgas, P. Singh, L.G. Leal, Computational studies of nonlinear elastic dumbbell models of Boger fluids in a cross-slot flow, J. Non-Newt. Fluid Mech. 88 (1999) 31–61, http://dx.doi.org/10.1016/S0377-0257(99)00020-8.
[9] R.G. Larson, Instabilities in viscoelastic flows, Rheol. Acta 31 (1992) 213–263, http://dx.doi.org/10.1007/BF00366504.
[10] E.S.G. Shaqfeh, Purely elastic instabilities in viscometric flows, Annu. Rev. Fluid Mech. 28 (1996) 129–185, http://dx.doi.org/10.1146/annurev.fl.28.010196.001021.
[11] J.A. Pathak, S.D. Hudson, Rheo-optics of equilibrium polymer solutions: wormlike micelles in elongational flow in a microfluidic cross-slot, Macromolecules 39 (2006) 8782–8792, http://dx.doi.org/10.1021/ma061355r.
[12] S.J. Haward, G.H. McKinley, Stagnation point flow of wormlike micellar solutions in a microfluidic cross-slot device: effects of surfactant concentration and ionic environment, Phys. Rev. E 85 (2012) 031502, http://dx.doi.org/10.1103/PhysRevE.85.031502.
[13] N. Dubash, P. Cheung, A.Q. Shen, Elastic instabilities in a microfluidic cross-slot flow of wormlike micellar solutions, Soft Matter 8 (2012) 5847–5856, http://dx.doi.org/10.1039/c2sm25215e.
[14] S.J. Haward, T.J. Ober, M.S.N. Oliveira, M.A. Alves, G.H. McKinley, Extensional rheology and elastic instabilities of a wormlike micellar solution in a microfluidic cross-slot device, Soft Matter 8 (2012) 536–555, http://dx.doi.org/10.1039/c1sm06494k.
[15] G.N. Rocha, R.J. Poole, M.A. Alves, P.J. Oliveira, On extensibility effects in the cross-slot flow bifurcation, J. Non-Newt. Fluid Mech. 156 (2009) 58–69, http://dx.doi.org/10.1016/j.jnnfm.2008.06.008.
[16] R.G. Larson, E.S.G. Shaqfeh, S.J. Muller, A purely elastic instability in Taylor–Couette flow, J. Fluid Mech. 218 (1990) 573–600, http://dx.doi.org/10.1017/S0022112090001124.
[17] G.H. McKinley, P. Pakdel, A. Öztekin, Rheological and geometric scaling of purely elastic flow instabilities, J. Non-Newt. Fluid Mech. 67 (1996) 19–47, http://dx.doi.org/10.1016/S0377-0257(96)01453-X.
[18] M.S.N. Oliveira, F.T. Pinho, R.J. Poole, P.J. Oliveira, M.A. Alves, Purely elastic flow asymmetries in flow-focusing devices, J. Non-Newt. Fluid Mech. 160 (2009) 31–39, http://dx.doi.org/10.1016/j.jnnfm.2009.02.010.
[19] L. Xi, M.D. Graham, A mechanism for oscillatory instability in viscoelastic cross-slot flow, J. Fluid Mech. 622 (2009) 145, http://dx.doi.org/10.1017/S0022112008005119.
[20] A. Afonso, M.A. Alves, F.T. Pinho, Purely elastic instabilities in three-dimensional cross-slot geometries, J. Non-Newt. Fluid Mech. 165 (2010) 743–751, http://dx.doi.org/10.1016/j.jnnfm.2010.03.010.
[21] J. Soulages, M.S.N. Oliveira, P.C. Sousa, M.A. Alves, G.H. McKinley, Investigating the stability of viscoelastic stagnation flows in T-shaped microchannels, J. Non-Newt. Fluid Mech. 163 (2009) 9–24, http://dx.doi.org/10.1016/j.jnnfm.2009.06.002.
[22] A.M. Afonso, P.J. Oliveira, F.T. Pinho, M.A. Alves, Dynamics of high-Deborah-number entry flows: a numerical study, J. Fluid Mech. 677 (2011) 272–304, http://dx.doi.org/10.1017/jfm.2011.84.
[23] M.A. Hulsen, R. Fattal, R. Kupferman, Flow of viscoelastic fluids past a cylinder at high Weissenberg number: stabilized simulations using matrix logarithms, J. Non-Newt. Fluid Mech. 127 (2005) 27–39, http://dx.doi.org/10.1016/j.jnnfm.2005.01.002.
[24] H.J. Wilson, Open mathematical problems regarding non-Newtonian fluids, Nonlinearity 25 (2012) R45–R51, http://dx.doi.org/10.1088/0951-7715/25/3/R45.
[25] R. Lagnado, N. Phan-Thien, L. Leal, The stability of two-dimensional linear flows of an Oldroyd-type fluid, J. Non-Newt. Fluid Mech. 18 (1985) 25–59, http://dx.doi.org/10.1016/0377-0257(85)85010-2.
[26] N. Phan-Thien, A nonlinear network viscoelastic model, J. Rheol. 22 (1978) 259, http://dx.doi.org/10.1122/1.549481.
[27] M.A. Alves, R.J. Poole, Divergent flow in contractions, J. Non-Newt. Fluid Mech. 144 (2007) 140–148, http://dx.doi.org/10.1016/j.jnnfm.2007.04.003.
[28] J. Zilz, R.J. Poole, M.A. Alves, D. Bartolo, B. Levanché, A. Lindner, Geometric scaling of a purely elastic flow instability in serpentine channels, J. Fluid Mech. 712 (2012) 203–218, http://dx.doi.org/10.1017/jfm.2012.411.
[29] R. Fattal, R. Kupferman, Constitutive laws for the matrix-logarithm of the conformation tensor, J. Non-Newt. Fluid Mech. 123 (2004) 281–285, http://dx.doi.org/10.1016/j.jnnfm.2004.08.008.
[30] A. Afonso, P.J. Oliveira, F.T. Pinho, M.A. Alves, The log-conformation tensor approach in the finite-volume method framework, J. Non-Newt. Fluid Mech. 157 (2009) 55–65, http://dx.doi.org/10.1016/j.jnnfm.2008.09.007.
[31] P.J. Oliveira, F.T. Pinho, G.A. Pinto, Numerical simulation of non-linear elastic flows with a general collocated finite-volume method, J. Non-Newt. Fluid Mech. 79 (1998) 1–43, http://dx.doi.org/10.1016/S0377-0257(98)00082-2.
[32] M.A. Alves, P.J. Oliveira, F.T. Pinho, A convergent and universally bounded interpolation scheme for the treatment of advection, Int. J. Numer. Meth. Fluids 41 (2003) 47–75, http://dx.doi.org/10.1002/fld.428.
[33] J.H. Ferziger, M. Perić, Further discussion of numerical errors in CFD, Int. J. Numer. Meth. Fluids 23 (1996) 1263–1274, http://dx.doi.org/10.1002/(SICI)1097-0363(19961230)23:12<1263::AID-FLD478>3.0.CO;2-V.
[34] J.M. Rallison, E.J. Hinch, Do we understand the physics in the constitutive equation?, J Non-Newt. Fluid Mech. 29 (1988) 37–55, http://dx.doi.org/10.1016/0377-0257(88)85049-3.